PERGAMON

International Journal of Heat and Mass Transfer 42 (1999) 971–991

International Journal of
HEAT and MASS
TRANSFER

A probability density function approach to modeling turbulence–radiation interactions in nonluminous flames

Sandip Mazumder[a], Michael F. Modest[b,*]

[a] *CFD Research Corporation, 215 Wynn Drive, Huntsville, AL 35805, U.S.A.*
[b] *Department of Mechanical Engineering, The Pennsylvania State University, 208 Reber Building, University Park, PA 16802, U.S.A.*

Received 29 April 1997; in final form 10 July 1998

Abstract

The interactions between turbulence and radiation, although acknowledged and qualitatively understood over the last several decades, are extremely difficult to model. Traditional Eulerian turbulence models are incapable of addressing the ‘closure problem’ for any realistic reactive flow situation, on account of the large number of unknown turbulent moments. A novel approach, based on the velocity-composition joint probability density function (PDF) method, has been used to attain closure. The ability of this method to accurately determine any one-point scalar correlation makes it a suitable candidate for modeling turbulence–radiation interactions (TRI). Results presented for a bluff-body-stabilized methane–air diffusion flame demonstrate the importance of turbulence–radiation interactions in flame calculations.

Nomenclature

B	width of bluff-body (Fig. 1)
$c_{p\alpha}$	specific heat of α-th species at constant pressure
c_{pmix}	mixture specific heat at constant pressure
C_ϕ	constant in Dopazo's model, $=2$
D	width of fuel injector (Fig. 1)
E_a	activation energy of fuel
G_η	spectral incident radiation
h_α	total enthalpy of αth species
$\Delta \mathrm{h}$	sensible enthalpy
$h^0_{\mathrm{f}\alpha}$	enthalpy of formation of the αth species at the standard state
I_η	spectral radiative intensity
$I_{\mathrm{b}\eta}$	Planck function
k	turbulent kinetic energy
M_α	molecular weight of αth species
M_{mix}	mixture molecular weight
N	total number of scalars
N_b	total number of molecular gas bands
N_c	total number of particles in a given cell
$\underline{q}^\mathrm{C}$	convective heat flux vector
$\underline{q}^\mathrm{R}$	radiative heat flux vector
R_u	universal gas constant
Re	Reynolds number
s	position
$\hat{s}$	unit vector along a line of sight
S_{chem}	source term in energy transport equation due to chemical reaction
S_α	source due to chemical reaction and radiation in αth scalar transport equation
t	time
T	temperature
T_0	standard state temperature
U_i	velocity in the ith direction
$U_{\mathrm{a,in}}$	inlet axial velocity of air stream
$U_{\mathrm{f,in}}$	inlet axial velocity of fuel stream
W_i	isotropic Wiener process
x_i	space variable in ith direction
Y_α	mass-fraction of αth species.

Greek

ε	rate of dissipation of k
ε_w	emissivity of wall
η	wave number
Γ_α	generic kinematic diffusivity of αth scalar

---

[*] Corresponding author. Tel.: 001 814 863 0976; fax: 001 814 863 8682; e-mail: mfm@mara.me.psu.edu

0017–9310/98/$—see front matter © 1998 Elsevier Science Ltd. All rights reserved
PII: S0017-9310(98)00225-7

κ_η spectral absorption coefficient
κ_i equivalent box height of ith absorption band
ν kinematic viscosity
ϕ_α αth scalar
$\underline{\phi}$ set consisting of all scalars
Φ_{in} inlet equivalence ratio
ρ mixture density
$\rho_{a,\mathrm{in}}$ inlet density of air stream
τ turbulent time-scale
τ_R reaction time-scale.

1. Introduction

Turbulent flames are characterized by large fluctuations in temperature and concentrations. The fluctuations often range between 40–65% of the mean [1, 2]. The spectral radiative absorption coefficient of a mixture of gases is a function of the temperature and concentration of the gas mixture and, therefore, is characterized by large fluctuations, as well. These fluctuations interact with fluctuations in the Planck function (a function of temperature) and the radiative intensity. These interactions are typically referred to as 'turbulence–radiation interactions' (TRI).

The interaction between radiation and turbulence is now a well-acknowledged phenomenon. Over the last two decades or so, a substantial amount of research effort has been directed toward this area. In the seventies and eighties, it has been shown by analysis [3–10] that an interaction between turbulence and radiation does exist. The answer to the question as to how these interactions affect radiative heat fluxes and divergence of radiative heat fluxes is still a matter of conjecture and argument. The earliest numerical calculations were undertaken by Germano [7]. His calculations were based on the assumption that the scalar fluctuations are random and the medium is gray. Although far from the truth, the calculations based on these assumptions did prove that TRI exists. Pearce and Varma performed similar calculations for the 4.3 μm CO_2 band. In their approach, the optical paths were broken up into a number of statistically independent homogeneous segments. The two-point statistical correlations were then described by assuming exponential correlation functions. This approach was later adopted by Chan and Chern [11] and by Faeth and coworkers [12–15]. In these numerical investigations, the hydrodynamic and scalar fields were obtained by a mixture-fraction formulation and the k-ϵ-g model. Kounalakis et al. [13] have used experimentally measured radiative intensities in conjunction with a stochastic time-series method and concluded that TRI enhances heat transfer rates in turbulent non-luminous diffusion flames by a factor of 1.1 to 4.2. This, however, appears to be in contrast with their earlier work [15], where the effect of TRI was deemed insignificant. Song and Viskanta [10] and Soufiani et al. [9] have also performed calculations that show that TRI can enhance heat loads on combustor walls. In recent years, calculations performed by Adams and Smith [16] for luminous flames have also demonstrated the importance of TRI in flame computations.

The evaluation of the unknown terms arising out of turbulence-radiation interactions poses considerable difficulties in Eulerian closure schemes. It essentially reduces to the evaluation of the correlations $\langle T'^2 \rangle$ and $\langle Y'_\alpha T' \rangle$, for $\alpha = 1, 2, 3, \ldots, N-1$, where $N-1$ is the total number of species with mass-fractions Y_α. This can be shown by performing a Taylor series expansion of the spectral absorption coefficient and the Planck function about their mean values, and then averaging the resultant product after linearization. The correlations $\langle T'^2 \rangle$ and $\langle Y'_\alpha T' \rangle$ can be obtained by deriving transport equations for these quantities and then modeling the right-hand-side of the resulting transport equations although such modeling is extremely cumbersome. Even if the transport equations were available in modeled form, one would still have to solve a whole set of additional non-linear partial differential equations. With any realistic chemistry, the problem soon becomes numerically intractable. It can be shown further that the evaluation of $\langle Y'_\alpha T' \rangle$ by the traditional transport-equation approach requires the evaluation of the correlations $\langle Y'_\alpha Y'_\beta \rangle$ for all values of α and β [17].

As opposed to traditional Eulerian closure methodologies, stochastic approaches, such as the velocity-composition joint probability density function (PDF) method [18, 19] can overcome most of the above problems with relative ease. As a first step in the velocity-composition joint PDF approach, a joint PDF transport equation is derived by combining all conservation equations. The fluid within the whole computational domain is then discretized into representative samples (or 'particles'). These particles move within the domain with time following certain governing equations, which essentially are the Lagrangian equations of motion. The particles carry with them all passive scalars as well, whose magnitudes are determined by solving the Lagrangian scalar transport equations of the particles. The Eulerian mean quantities are obtained by sampling these particles in spatial bins, and then averaging. Since the approach is Lagrangian, convective transport is treated without any approximation or modeling and, therefore, the question of modeling the turbulent flux terms arising from averaging the nonlinear advective terms in traditional schemes does not arise. Also, this eliminates the critical problem of numerical diffusion associated with traditional finite-volume schemes. In such approaches, modeling is required only for closure of the fluctuating pressure-strain-rate terms, as well as the dissipation terms, and is performed using stochastic processes. A comprehensive discussion of the velocity-composition joint PDF method and its underlying theory may be found in the review paper by Pope [19] and the references cited therein.

This article presents a novel approach to accounting to TRI in confined turbulent flames. The approach presented here accounts for all aspects of a general turbulent reactive flow, namely, turbulent fluid flow, finite-rate kinetics, multiple gas-band radiative calculations and the treatment of interactions between turbulence and radiation. Assumptions, associated with the modeling of turbulence-chemistry interactions, namely 'fast' or 'slow' chemistry (this governs the ratio of the reaction to the turbulent time scale) have been eliminated. Also, it is not necessary to use unity Lewis or Schmidt numbers, and is applicable to both premixed and diffusion flame computations. The models and approximations adopted here, by no means, restrict the capability of the overall approach. For example, detailed chemistry, detailed nongray models, and likewise, alternate solution approaches for the radiative transfer equation can be implemented without reworking the formulation. The objective of this article is not to present accurate flame calculation results, but rather to present a general, powerful modeling technique that may be used for a wide variety of combustion applications to treat turbulence–radiation interactions.

2. Mathematical description

2.1. *Turbulence–radiation interactions* (*TRI*)

The radiative transfer equation (RTE) for a nonscattering medium [20] is:

$$\frac{\partial I_\eta}{\partial s} = \kappa_\eta (I_{b\eta} - I_\eta), \tag{1}$$

where I_η is the spectral radiative intensity, κ_η is the spectral absorption coefficient, and $I_{b\eta}$ is the Planck function. The time-constant for radiative transport in an enclosure of characteristic dimension of a meter is in the order of a few tens of nanoseconds. This is considerably faster than the fastest chemical reactions, whose time-constants are typically in the order of microseconds and, therefore, the transient term in the radiative transfer equation has been neglected. The spectral absorption coefficient, Planck function, and spectral intensity are decomposed into a mean and a fluctuating part:

$$\kappa_n = \langle \kappa_\eta \rangle + \kappa'_\eta, \quad I_\eta = \langle I_\eta \rangle + I'_\eta, \quad \text{and} \quad I_{b\eta} = \langle I_{b\eta} \rangle + I'_{b\eta}, \tag{2}$$

where the quantities within angled brackets denote ensemble averages and the quantities with primes denote fluctuations. Substitution of equation (2) into equation (1), followed by averaging yields

$$\frac{\partial \langle I_\eta \rangle}{\partial s} = \langle \kappa_\eta \rangle \langle I_{b\eta} \rangle - \langle \kappa_\eta \rangle \langle I_\eta \rangle + \langle \kappa'_\eta I'_{b\eta} \rangle - \langle \kappa'_\eta I'_\eta \rangle. \tag{3}$$

The last two terms in eqn (3) are additional terms that arise due to the interaction of radiation with turbulence. For closure, these terms need to be evaluated.

Researchers in the field of radiation–turbulence interaction have assumed that the correlation between the fluctuating absorption coefficient, κ'_η, and the fluctuating radiative intensity, I'_η, is negligible. Kabashnikov [4] has established a criterion, which states that this assumption is correct if the optical thickness of the radiating gas, based on the macroscale of turbulence, l, is small, i.e., $\langle \kappa_\eta \rangle l \ll 1$. This approximation is referred to as the 'optically thin fluctuation approximation' (OTFA). Kabashnikov and Myasnikova [3], and later Song and Viskanta [10], have provided physical arguments, which support this approximation. The idea has more recently been augmented by Hall and Vranos [8]. Thus, the only term that needs to be evaluated to attain closure is $\langle \kappa'_\eta I'_{b\eta} \rangle$. This is true in the vast majority of flames.

2.2. *Hydrodynamic transport*

The motion of individual particles is governed by the following set of ordinary differential equations given by Pope and coworkers [19, 21]:

$$\Delta U_i^* = -\frac{1}{\rho^*}\frac{\partial \langle p \rangle}{\partial x_i}\Delta t + 2\nu \frac{\partial^2 \langle U_i \rangle}{\partial x_j \partial x_j}\Delta t + \sqrt{2\nu}\Delta W_j \frac{\partial \langle U_i \rangle}{\partial x_j} + G_{ij}(U_j^* - \langle U_j \rangle)\Delta t + \sqrt{C_0 \varepsilon}\Delta W'_i,$$

and

$$\Delta x_i^* = U_i^* \Delta t + \sqrt{2\nu}\Delta W_i \quad i = 1, 2, 3 \tag{4}$$

where U_i^* is the particle velocity, and x_i^* is the particle position. Quantities within angled brackets represent Eulerian averages, which, in the current context of reactive flows, are Favre averages. The first term in equation (4) represents transport by the mean pressure gradient; the second and third terms describe molecular transport, and are usually negligible at large Reynolds numbers except in the vicinity of solid walls. The last two terms, in conjunction, provide a stochastic representation of transport by the fluctuating pressure gradient and viscous dissipation of the turbulent fluctuations, and have been structured after the Generalized Langevin Model (GLM) [21]. The function $\Delta W_i(t)$ is the change in an isotropic Wiener process. The Wiener process is a non-differentiable function which, when integrated over time, results in a random number drawn from a standardized Gaussian distribution whose mean is zero and whose variance is equal to the time interval over which the function has been integrated. Expression for the tensor G_{ij} may be obtained from Haworth and Pope [21].

2.3. *Scalar transport*

The Lagrangian transport of any passive scalar is governed by the following set of ordinary differential equations [17, 19, 22, 23]:

$$\Delta\phi_\alpha^* = (\Gamma_\alpha + \nu)\frac{\partial^2\langle\phi_\alpha\rangle}{\partial x_j\,\partial x_j}\Delta t + \sqrt{2\nu}\Delta W_j\frac{\partial\langle\phi_\alpha\rangle}{\partial x_j}$$
$$-\frac{C_\phi}{2\tau}(\phi_\alpha^* - \langle\phi_\alpha\rangle)\Delta t + S_\alpha(\underline{\phi}^*) \quad \alpha = 1,2,\ldots,N, \qquad (5)$$

where ϕ_α^* is the αth scalar of an individual particle ($\alpha = 1,2,\ldots,N-1$ for the mass-fractions of $N-1$ species, and $\alpha = N$ for temperature), and Γ_α is the molecular diffusivity of the αth scalar. The first two terms in eqn (5) represent molecular transport. The third term describes dissipation of the scalar fluctuations (turbulent mixing), and is attributed to Dopazo [22]. The constant, C_ϕ, assumes a value close to 2, and a discussion to this effect may be found in Mazumder and Modest [23] and the references cited therein. The last term in equation (5) is the source due to chemical reaction and radiation, and is written as:

$$S_\alpha = \begin{cases} \displaystyle\int_{\Delta t}\frac{\mathrm{d}Y_\alpha^*}{\mathrm{d}t}\mathrm{d}t & \alpha = 1,2,\ldots,N-1 \\ \displaystyle\int_{\Delta t} S_{\mathrm{chem}}^*\,\mathrm{d}t - (\nabla\cdot\underline{q}^{\mathrm{R}})\Delta t & \alpha = N. \end{cases} \qquad (6)$$

The determination of $\mathrm{d}Y_\alpha^*/\mathrm{d}t$ and S_{chem} will be discussed later.

The above set of equations, in conjunction with the equation of state, completely describes the path and composition of a particle at any given time starting from an initial state. If the low Mach number assumption is invoked, the effects of pressure are decoupled, and the equations are coupled to each other through the density only. It is also reasonable to assume that the reference pressure does not change with time, which is true for most combustion applications except internal combustion engines. We will restrict ourselves to the case where the reference pressure does not change as a function of time, although the procedure is also applicable to truly compressible flows (except that, in such a case, the solution for the pressure field gets considerably more complicated).

As a particle travels, it may approach a solid wall. In the vicinity of a solid wall, viscous effects comes into play, and equations (4) need to be modified. These modifications have been outlined in detail by Mazumder and Modest [23, 24]. The detailed solution algorithm may be found in Mazumder [17].

2.4. Chemical reaction

Methane is the most important constituent of natural gases and, therefore, has been chosen as the fuel in the current study. Methane produces soot only under excessively rich conditions and is, thus, an ideal fuel for studies of non-luminous flames. A wide range of chemical kinetic models for methane are available in the literature. In this study, the simplest form, i.e., a single-step Arrhenius rate will be adopted. The single-step reaction of oxidation of methane may be written as:

$$\mathrm{CH_4} + 2\mathrm{O_2} \rightarrow \mathrm{CO_2} + 2\mathrm{H_2O}. \qquad (7)$$

Westbrook and Dryer [25] provide an Arrhenius relationship for the reaction-rate of methane as:

$$\frac{\mathrm{d}[\mathrm{CH_4}]}{\mathrm{d}t} = -A\exp(-E_a/R_uT)[\mathrm{CH_4}]^a[\mathrm{O_2}]^b, \qquad (8)$$

where the quantities within square brackets represent molar concentrations; R_{u} is the universal gas constant, and E_{a} is the activation energy of methane. A, a and b are unknown constants in the general Arrhenius equation, which may be obtained from Westbrook and Dryer [25].

The rate of production/destruction of heat due to chemical reactions requires special consideration. The contributions by reaction, dissipation, molecular transport and radiation are treated sequentially within a single time-step. The chemical energy in an individual particle is first transformed to sensible energy, which is then allowed to change by heat transfer from the particle by various mechanisms. The heat released by reaction in a single particle can be computed by treating the particle as an adiabatic control mass and a perfectly stirred reactor model [19]. Under this assumption (and assuming a constant pressure process, which is consistent with the low Mach number assumption discussed earlier), the First Law for an individual particle reduces to

$$\frac{\mathrm{d}h}{\mathrm{d}t} = \frac{\mathrm{d}}{\mathrm{d}t}\left[\sum_\alpha Y_\alpha h_\alpha\right] = 0, \qquad (9)$$

where the superscript '*' (representative of a particle) has been omitted to keep the notation simple. The enthalpy of the αth species, by definition, is

$$h_\alpha = h_{\mathrm{f}\alpha}^0 + \textstyle\int_{T_0}^{T} c_{\mathrm{p}\alpha}(T)\,\mathrm{d}T, \qquad (10)$$

where $h_{\mathrm{f}\alpha}^0$ is the enthalpy of formation of the standard state, T_0 is the temperature at the standard state, and $c_{\mathrm{p}\alpha}$ is the specific heat at constant pressure. The second term in equation (10) represents the sensible enthalpy measured against the standard state, and is often denoted by Δh_α.

In order to determine the temperature from the enthalpy, the integral relation in equation (10) must be inverted. This is commonly performed by interpolation. Another common scheme for flame computations is to assume $c_{\mathrm{p}\alpha}$ to be a constant, evaluated at an elevated temperature, so that a fairly accurate answer is obtained. For purposes of the current study, the second approach was deemed adequate, and the value of the specific heat at 1500 K was used. Equation (10), along with the assumption of constant specific heats, when substituted into equation (9) yields

$$S_{\text{chem}} = -\sum_{\alpha=1}^{N-1} h_\alpha \frac{\mathrm{d}Y_\alpha}{\mathrm{d}t} = -\sum_{\alpha=1}^{N-1} h^0_{\mathrm{f}\alpha}\frac{\mathrm{d}Y_\alpha}{\mathrm{d}t} - (T-T_0)\sum_{\alpha=1}^{N-1} c_{\mathrm{p}\alpha}\frac{\mathrm{d}Y_\alpha}{\mathrm{d}t} = c_{\text{pmix}}\frac{\mathrm{d}T}{\mathrm{d}t}, \quad (11)$$

where c_{pmix} is the mixture specific heat for a particle ($=\Sigma_\alpha Y_\alpha c_{\mathrm{p}\alpha}$), and $N-1$ is the total number of species.

Equations (8) and (11), in conjunction with the rate equations for the other species, form a set of non-linear, implicitly-coupled ordinary differential equations (ODEs). In the current context, Gear's method [26] was used to solve the set of ODEs.

In the particle-tracing Lagrangian scheme, each particle has its own composition, i.e., its own temperature and species mass-fractions and, therefore, its own density, specific heat and molecular weight. This implies that all one-point statistics of the scalars are preserved by this approach. Since reaction depends only on one-point statistics of the scalars, this approach enables exact treatment of reactions, i.e., no model is necessary to treat turbulence-chemistry interactions. Clearly, this is one of the strengths of the PDF approach, since in Eulerian approaches an assumption regarding the relative magnitudes of the reaction and turbulent time-scales is required to evaluate the average source term at each cell center.

2.5. Thermal radiation

Equation (3) is a directional equation, and is difficult to solve in its present form even if the TRI terms are known. One strategy that is often employed is the use of the P_1-approximation, which reduces this directional equation to a Helmholtz equation [20] for the integrated (over all directions) incident radiation, G_η. The transport equation for the incident radiation [20], after decomposing into mean and fluctuating parts and averaging, may be written as

$$\nabla\left(\frac{1}{3\langle\kappa_\eta\rangle}\nabla\langle G_\eta\rangle\right) = -4\pi(\langle\kappa_\eta\rangle\langle I_{\mathrm{b}\eta}\rangle + \langle\kappa'_\eta I'_{\mathrm{b}\eta}\rangle) + \langle\kappa_\eta\rangle\langle G_\eta\rangle, \quad (12)$$

subject to the boundary condition

$$\hat{n}\cdot\langle \underline{q}^{\mathrm{R}}_{\mathrm{w}\eta}\rangle = -\left[\frac{1}{3\langle\kappa_\eta\rangle}\hat{n}\cdot\nabla\langle G_\eta\rangle\right]_{\mathrm{w}} = \frac{\epsilon_{\mathrm{w}}}{2(\epsilon_{\mathrm{w}}-2)}[4\pi I_{\mathrm{bw}\eta} - G_{\mathrm{w}\eta}], \quad (13)$$

where $\underline{q}^{\mathrm{R}}$ is the net radiative heat flux, $\hat{n}$ is a unit vector normal to the wall, and ε_{w} is the emissivity of the wall. All quantities with the subscript 'w' imply that they are evaluated at the wall. The correlation between G'_η and κ'_η has been neglected following arguments presented earlier. The internal source due to radiation, which appears in equation (6) for $\alpha = N$ is equal to the negative of the divergence of the radiative heat flux, and is expressed as [20]

$$-\langle\nabla\cdot\underline{q}^{\mathrm{R}}\rangle = -\int_0^\infty [4\pi(\langle\kappa_\eta\rangle\langle I_{\mathrm{b}\eta}\rangle + \langle\kappa'_\eta I'_{\mathrm{b}\eta}\rangle) - \langle\kappa_\eta\rangle\langle G_\eta\rangle]\,\mathrm{d}\eta = -\sum_{k=1}^{N_{\mathrm{b}}}[4\pi(\langle\kappa\rangle_k\langle I_{\mathrm{b}}\rangle_k + \langle\kappa' I'_{\mathrm{b}}\rangle_k) - \langle\kappa\rangle_k\langle G\rangle_k], \quad (14)$$

In the current study, the spectral variation of the absorption coefficient of the combustion gases was treated using wide-band models. The wind-band model data used here are a collection of data provided by Edwards [27] and Modak [28]. An excellent summary of all these data may be found in the text by Modest [20]. In the 'box model', the gas bands are modeled as rectangular boxes, within which the absorption coefficient is a constant (the box-height). The box-height and width can be determined from wide-band data following the procedure of Modest and Sikka [29].

Prior to solving equation (12) it is necessary to calculate the average absorption coefficient and the TRI terms for each cell and for each band. The band strengths and widths are functions of the temperature and composition field of the gas layer in question. For non-isothermal gas layers, the band widths and strengths are different at different spatial location. In order to solve equation (12), however, the set of band widths need to be the same over the entire computational domain. This is ensured by calculating the band-widths using a single characteristic value for temperature and composition. Although some accuracy is lost this way, it is unavoidable when solving the radiative transfer equation for a non-isothermal reactive gas layer by the simplified box model.

In the current particle-tracing scheme, since each particle has its own scalar field, the band strengths are computed for each particle based on the particle's own temperature and concentrations. Spatial averaging then yields the average band strength (box height) at each cell location. The deviation of the actual particle band strength from the average provides the fluctuating absorption coefficient. The TRI term for a given box, $\langle\kappa' I'_{\mathrm{b}}\rangle_k$, is calculated as

$$\langle\kappa' I'_{\mathrm{b}}\rangle_k = \frac{1}{N_{\mathrm{c}}}\sum_{n=1}^{N_{\mathrm{c}}}[\kappa^*_{nk} - \langle\kappa\rangle_k]\,[I^*_{\mathrm{b},n,k} - \langle I_{\mathrm{b}}\rangle_k], \qquad k = 1, 2, \ldots, N_{\mathrm{b}} \quad (15)$$

where N_{c} is the number of particles in the cell in question, and N_{b} is the total number of bands.

3. Results and discussion

Bluff bodies are often used in practical burners to anchor diffusion flames. In addition, the behavior and characteristics of bluff-body-stabilized flames have been investigated experimentally by a number of researchers in the past. Notable amongst these studies are the ones by Rocquemore et al. [30], Lee and Onuma [31], Masri and Bilger [32], and Kelly and co-workers [33, 34]. The geometry used for the simulations in the current study has been illustrated in Fig. 1. The dimensions shown in the figure were unchanged for all cases. The top and bottom walls, and the bluff-body were maintained isothermal at 700 K, and were considered gray, with an emissivity of 0.8. The air and fuel (methane, in this case) were injected at temperatures of 1200 K and 1000 K, respectively, and the inlets were assumed to be 'black' at these temperatures. The exit of the burner was also assumed 'black' at the local temperature of the exiting gas. The mean pressure field, was determined by solving the pressure-Poisson equation on a co-located grid using artificial dissipation [35]. The PISO algorithm [36] was implemented for pressure correction.

The simulations were performed primarily to study the effect of two important parameters: the inlet equivalence ratio, denoted by ϕ_{in}, and the Reynolds number, defined as: $Re = \langle \rho_{\text{a,in}} \rangle \langle U_{\text{a,in}} \rangle B/\mu$, where $\langle \rho_{\text{a,in}} \rangle$ is the mean inlet air density, $\langle U_{\text{a,in}} \rangle$ is the mean inlet air speed in the axial direction, and B is the width of the bluff-body (Fig. 1). The dynamic viscosity of the fluid, μ, was assumed to be that of air over the whole computational domain and its value at 1200 K was used everywhere. In order to facilitate easier referencing for future discussions, each case has been tabulated in Table 1, providing relevant information pertaining to each case, and has been assigned a number. In Table 1, $\langle U_{\text{f,in}} \rangle$ is the mean inlet fuel velocity. The inlet equivalence ratio can be changed by changing either the inlet flow velocity of the fuel jet, or by changing the inlet injection area of the fuel. Changing the flow speed is probably what an experimentalist would do (instead of using a variety of bluff bodies) to adjust the equivalence ratio and, therefore, the same strategy was adopted here.

Each simulation was performed with 100,000 particles and a 20×20 grid. The same grid was used for the finite-volume solution of the radiative transfer equation, as well as sampling in the Monte Carlo scheme.

For radiation calculations, ten molecular gas bands, centered around the following wavelengths, were chosen: 1.38 μm, 1.87 μm, 2.7 μm, 6.3 μm, and 71 μm bands for H_2O; 2.7 μm, 4.3 μm and 15 μm bands for CO_2; and 7.7 μm and 3.3 μm bands for CH_4.

Prior to extensive computations for the various cases mentioned above, the code was tested against experimental data provided by Kelly et al. [33]. In order to do so, a single simulation was performed in a 1.6 m long channel with $\langle U_{\text{a,in}} \rangle = 10\ \text{m s}^{-1}$ and $\langle U_{\text{f,in}} \rangle = 14\ \text{m s}^{-1}$, such that the ratio, $\langle U_{\text{f,in}} \rangle / \langle U_{\text{f,in}} \rangle = 1.4$. This is one of the cases that was investigated by Kelly et al. [33]. Kelly and co-workers indicate that the structure of the flame is not governed by the actual flow velocities, but rather, by the ratio of the velocities of fuel to air streams. A comparison of the methane concentrations at two different axial locations in the near-wake of the bluff-body have been shown in Fig. 2. The numerical data presented here are time-averaged data over approximately two 'periods'. The discrepancies between experimental and numerical results may be attributed to several factors. First, the fact that the experimental data are for a two-dimensional axisymmetric geometry and the numerical results are for a two-dimensional planar geometry will cause obvious differences. Although the rate of spread as

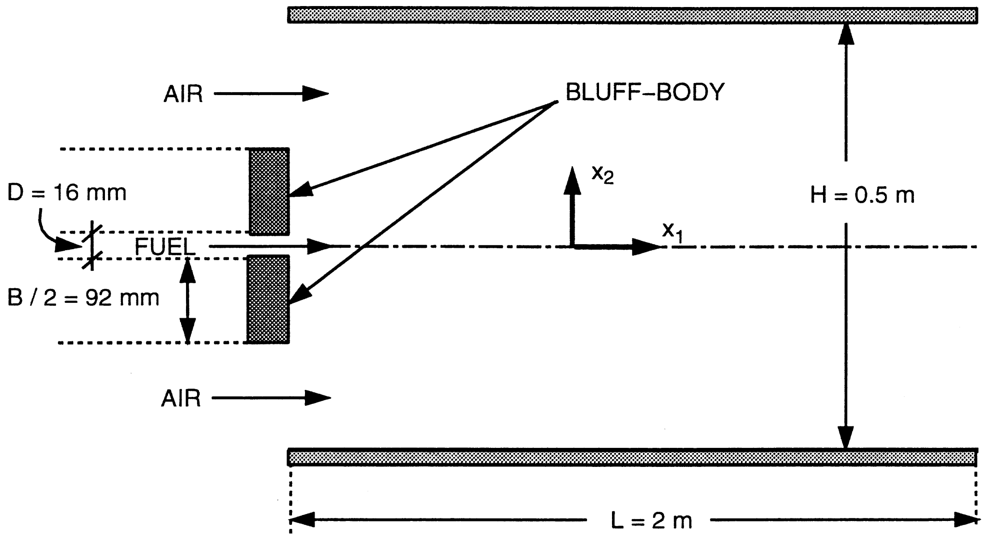

Fig. 1. Geometry of bluff-body burner used for sample calculations.

Table 1
Cases considered for the current study

Case No.	*Re*	Φ_{in}	Radiation?	TRI?	$\langle U_{a,in} \rangle$ (m/s)	$\langle U_{f,in} \rangle$ (m/s)	Δt (ms)
1	13,304	1.0	No	No	10.00	16.41	2.0
2	13,304	1.0	Yes	No	10.00	16.41	2.0
3	13,304	1.0	Yes	Yes	10.00	16.41	2.0
4	13,304	1.05	No	No	10.00	17.23	2.0
5	13,304	1.05	Yes	No	10.00	17.23	2.0
6	13,304	1.05	Yes	Yes	10.00	17.23	2.0
7	13,304	0.9	No	No	10.00	14.77	2.0
8	13,304	0.9	Yes	No	10.00	14.77	2.0
9	13,304	0.9	Yes	Yes	10.00	14.77	2.0
10	13,304	0.8	No	No	10.00	13.13	2.0
11	13,304	0.8	Yes	No	10.00	13.13	2.0
12	13,304	0.8	Yes	Yes	10.00	13.13	2.0
13	26,608	1.0	No	No	20.00	32.82	1.0
14	26,608	1.0	Yes	No	20.00	32.82	1.0
15	26,608	1.0	Yes	Yes	20.00	32.82	1.0
16	39,912	1.0	No	No	30.00	49.23	0.5
17	39,912	1.0	Yes	No	30.00	49.23	0.5
18	39,912	1.0	Yes	Yes	30.00	49.23	0.5

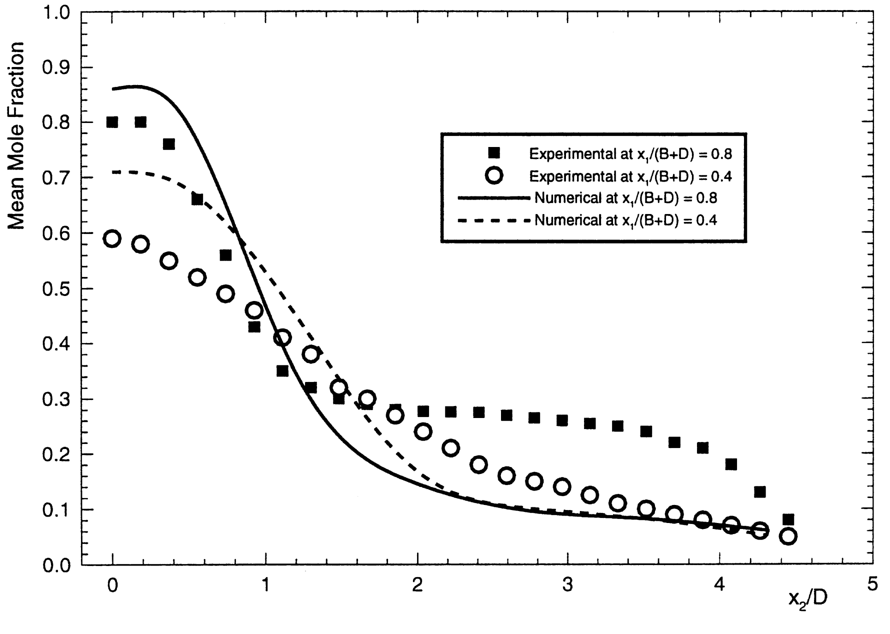

Fig. 2. Time-averaged methane concentration profiles in the near-wake region.

a function of axial distance of an axisymmetric jet is the same as the rate of spread of a planar jet, there are differences in spreading rates of similar wakes. Since the current scenario involved injection of a jet into a wake, the spreading rate of both streams in relevant. The diameter of an axisymmetric wake increases as the cube-root of axial distance from the bluff-body, while the width of a planar wake increases as the square-root of axial distance [37]. Thus, the size of a wake at a short distance from the bluff-body will be larger for an axisymmetric case than for a planar case. In the current context, this implies that for a planar wake the air stream will penetrate more towards the center of the bluff-body than for an axisymmetric wake, resulting in lower concentrations of fuel in the wake, especially at the outer edges of the bluff body. The second reason could be insufficient mixing in the wake. The flow pattern in the wake is complex, and it is possible that the Baldwin–Lomax model used here to calculate the dissipation rate is not adequate enough for regions close to the inlet, where the flow is strongly recirculating. This may be resulting in overprediction of the turbulent time scale, causing insufficient mixing of the fuel stream with the air stream. Furthermore, Dopazo's mixing model [22], which is used here, was developed for homogeneous turbulence. Although it has been modified to account for inhomogeneities near the walls, it does not account for inhomogeneities in the reaction zone. There is strong reason to believe that insufficient mixing is the cause of discrepancy between predicted and experimental results since the concentrations are overpredicted along the centerline and underpredicted along the edges.

3.1. General flame structure and characteristics

The recirculation behind the bluff-body anchors the flame. The co-flowing air jet entrains the fuel jet behind the bluff body, causing intense mixing and combustion. The coaxial flow of two jets with significantly different densities and momenta results in a well-known instability. In this case, the instability is further enhanced by combustion, which results in significant temperature and density gradients. Rocquemore et al. [30] specifically addressed instabilities associated with bluff-body-stabilized diffusion flames. They observed (for a propane–air flame at various flow rates) that downstream of the recirculation zone, the flame is pinched off to form discrete 'turbules' of varying size and shape. These turbules are created at a rate that is almost periodic, and move downstream at a speed almost equal to the inlet air speed. This experimentally observed behavior has been confirmed by the present simulation. The formation of flame turbules and their downstream march have been illustrated in a series of frames in Fig. 3 by showing temperature contours for Case 1 at various points in time. The first turbule begins for form approximately at 270 ms, and is pinched off completely from the tip of the flame at approximately 350 ms. During this time period, however, the primary flame changes shape from a blunt onion-like shape to a long dumbbell-like shape. The primary flame is observed to form two distinct lobes. This process continues and the length of the flame continues to grow until about 430 ms, at which point the second turbule is shed off. The final frame at 450 ms clearly shows the primary flame along with two turbules, which are almost equally spaced. These observations match closely with what was observed by Rocquemore et al. [30] in their experiments. The Strouhal number ($=f\times(B+D)/\langle U_{\mathrm{a,in}}\rangle$) based on the frequency of turbule shedding, f, was found to be approximately 0.2 (details in Mazumder [17]). In a recent article, Williamson [38] reported that the Strouhal number becomes independent of the Reynolds number once the flow becomes fully turbulent. Measurements taken by Williamson for cold flow show that the Strouhal number assumes a constant value of about 0.205 in the fully turbulent regime.

The distributions of the various species and the corresponding temperature distribution have been illustrated in the contour plots in Fig. 4, in which the profiles at 450 ms have been plotted for the same case as in the preceding figure.

The dynamic interactions between fluid entrainment, mixing, and combustion processes, which result in the instability, are undoubtedly complex, and can only be explained subjectively, at best. Rocquemore et al. [30] and also Lee and Onuma [31] postulate that the fuel jet penetrates into the region of intense combustion (just downstream of the 'neck' of the flame) in discrete, almost periodic, bursts, and that this is the root cause of turbule formation. This would imply that in the 'neck' region, which typically occurs at $x_1/D \simeq 10$ [39], the axial velocity at the centerline would be almost periodic. Data supporting this conjecture are shown in Fig. 5, which indicates a distinct periodic behavior in time of the velocity in question. The data shown in Fig. 5 are for Case 1. Similar behavior was also observed for all the other cases. Figure 3 shows that two turbules are formed between 270 and 450 ms, which is exactly equal to the number of crests or troughs observed to lie within that time interval in Fig. 5. This observation lends further support to the postulate of Rocquemore et al. [30] and Lee and Onuma [31].

In the presence of radiation and turbulence-radiation interactions, the overall behavior and structure of the flame remains almost the same. Noticeable differences, however, are observed in the flame temperatures. This has been illustrated in the series of frames in Fig. 6. Since the turbule formation process has already been demonstrated in Fig. 3, in this case only five frames are shown. The data presented here are for Case 3, which is identical to Case 1, except that thermal radiation and turbulence-radiation interactions were not neglected. In this case emission from the flame (to be quantified later) competes with heat release due to reaction. The net effect could produce a rise or fall in temperature depending on the relative strength of the two processes in question. Thus, the temperature of the marching turbules sometimes increase (as in the second turbule from 410 to 450 ms) and sometimes decrease (as in the first turbule from 290 ms onwards). Radiation appears as an important balancing mechanism: strong reaction produces high temperatures, in which case emission from the flame also becomes strong, and helps to keep the temperature under control.

Figure 7(a) shows a contour plot of the divergence of the radiative heat flux, which is essentially a measure of the net radiative emission from the flame. In regions where the flame is strongly emitting, the divergence is

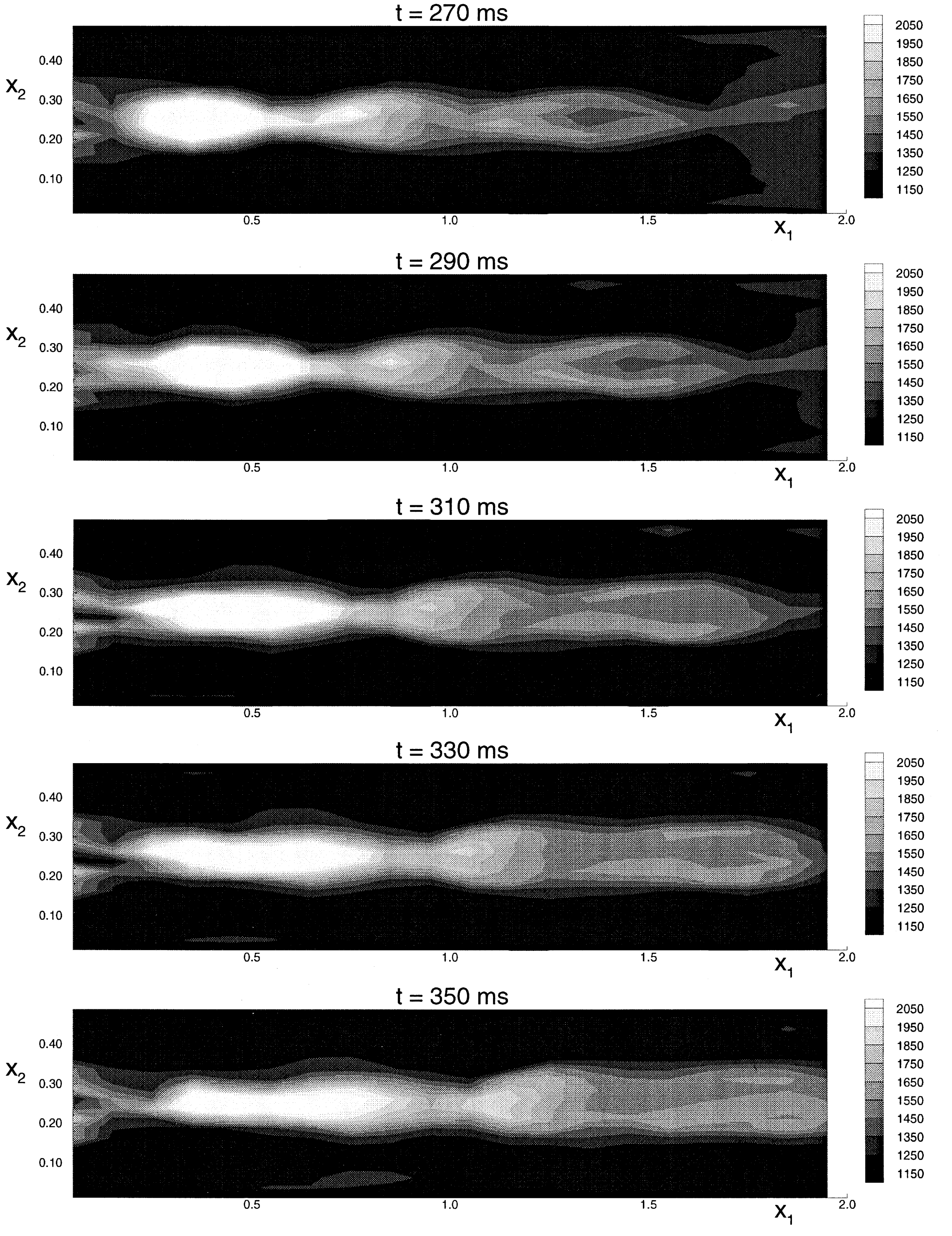

Fig. 3. Turbule formation (temperature contours shown here) with time.

large and positive, and in regions where the flame is absorbing, the divergence is negative. The data plotted in Fig. 7(a) are for Case 2, i.e. a case that does not take TRI into account. The dark shades indicate regions of strong emission, while the lighter shades indicate regions of absorption (negative divergence). The magnitude of

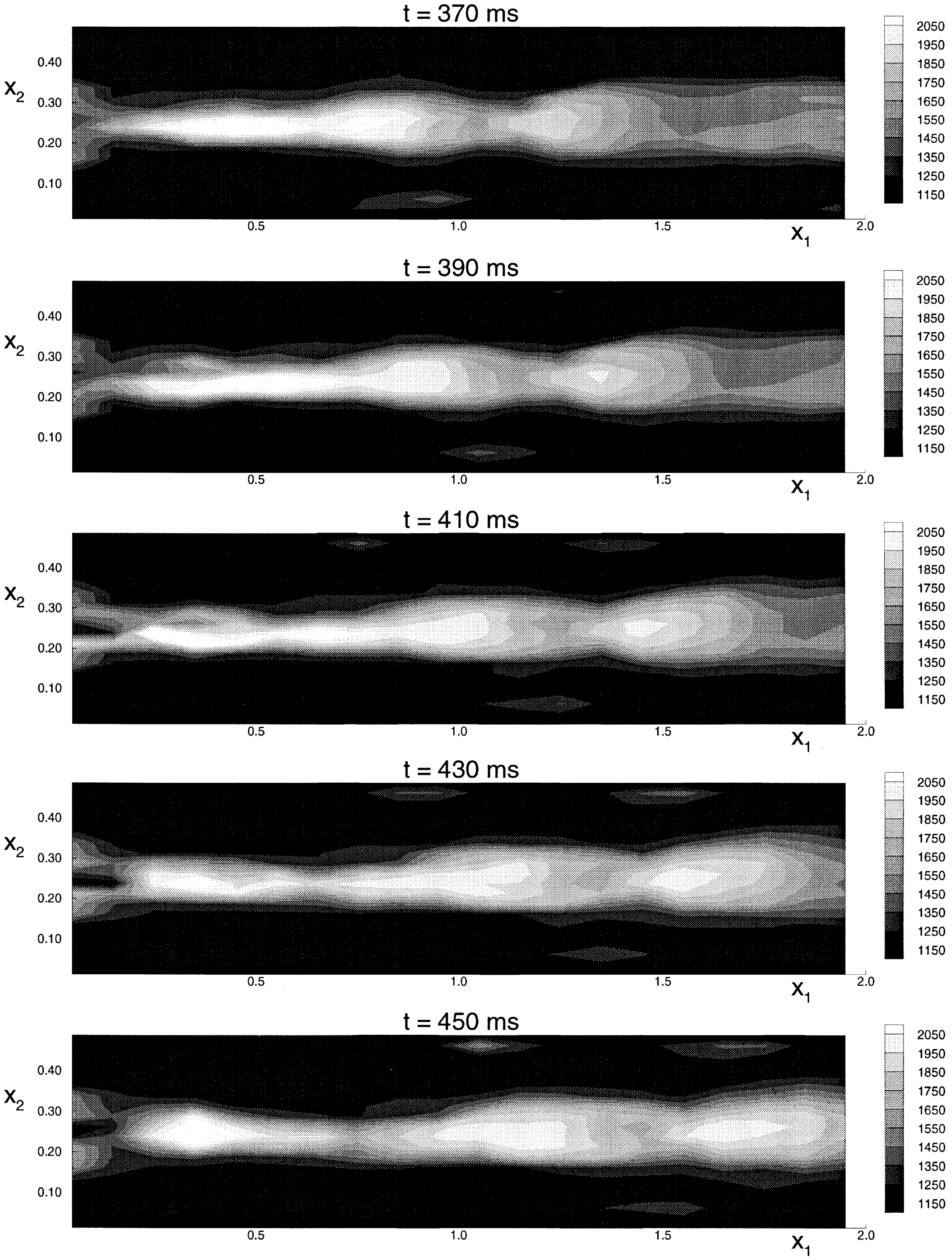

t = 370 ms

t = 390 ms

t = 410 ms

t = 430 ms

t = 450 ms

Fig. 3 (*continued*)

the maximum negative divergence is considerably smaller than the maximum positive divergence (by about two orders of magnitude), implying that although there are parts of the flame which do absorb energy by radiation, they are only weakly absorbing. The net effect is strong emission from the core of the flame, thereby producing

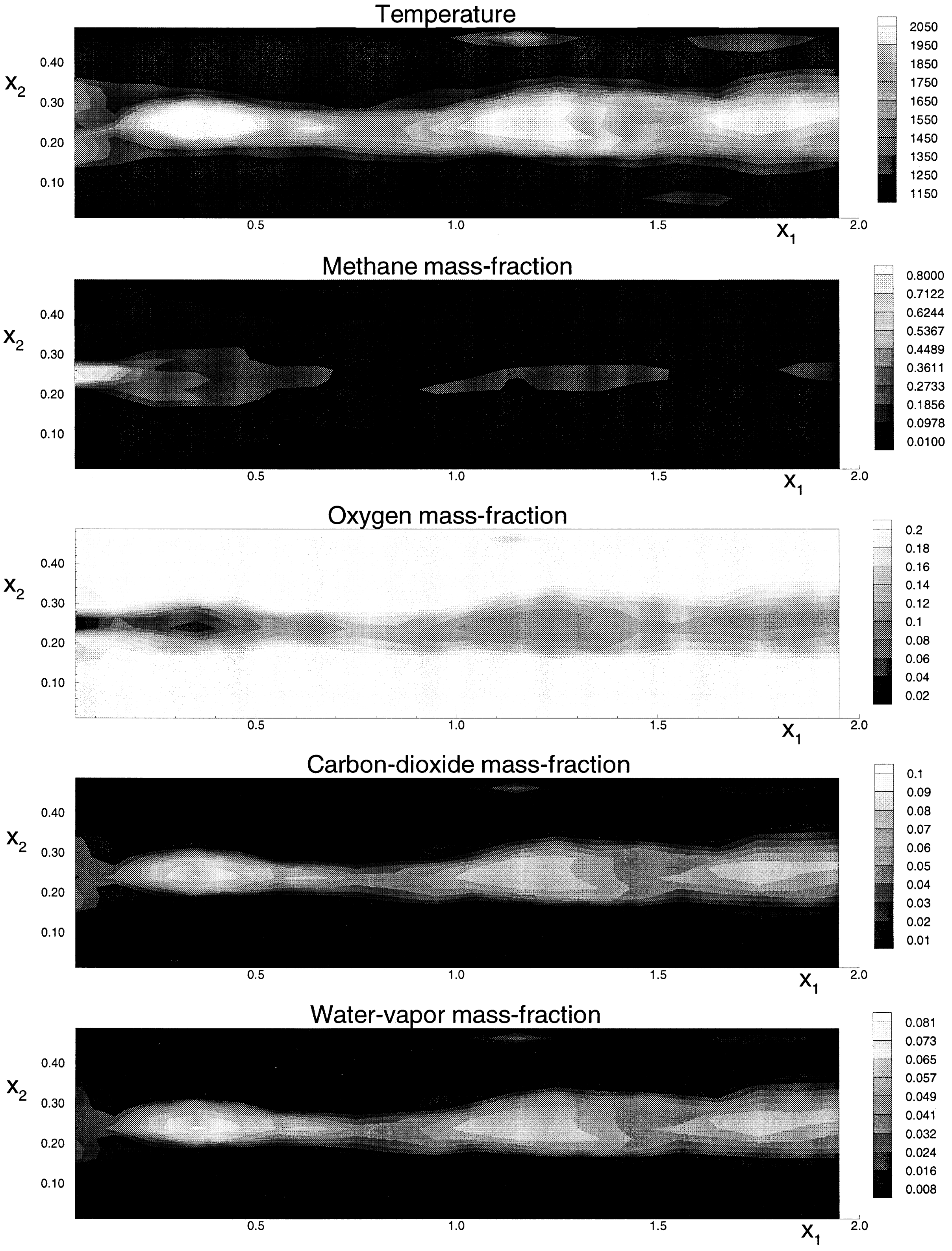

Temperature

Methane mass-fraction

Oxygen mass-fraction

Carbon-dioxide mass-fraction

Water-vapor mass-fraction

Fig. 4. Temperature and concentration profiles for Case 1 at 450 ms.

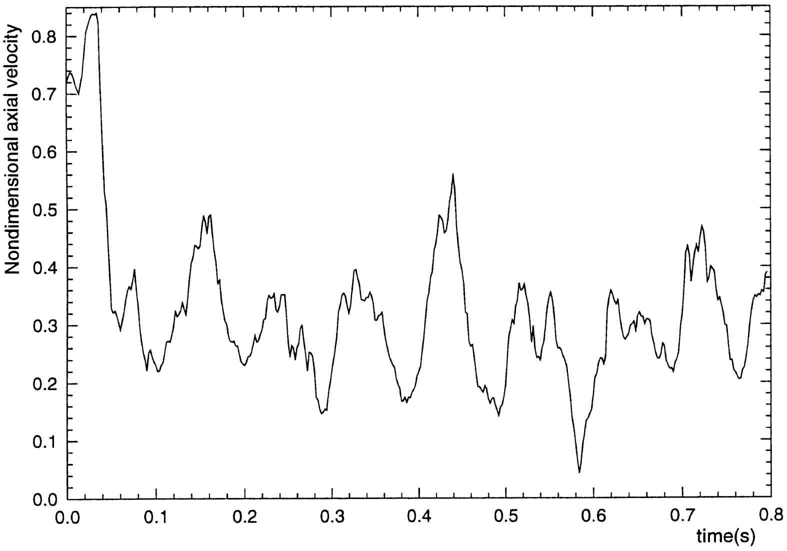

Fig. 5. Centerline nondimensional (normalized by $\langle U_{\mathrm{f,in}} \rangle$) axial velocity at $x_1/D = 9.375$ as a function of time.

the lower temperatures discussed earlier in this section.

Inclusion of TRI terms changes the entire flame structure, the temperature and composition fields, and the heat released due to reaction (since the reaction rate is dependent on temperature and compositions). This implies that a comparison of the divergences or any such quantities for the two cases at any given instant of time would be misleading. The effect of TRI can be best demonstrated, rather, by freezing a shot at any point in time, and then calculating the divergences first by turning off the TRI terms, and finally by turning them on. This approach isolates the effect of TRI on the flame emission and wall heat loads. In the current context, a restart file was generated after 460 ms for Case 2. The TRI terms were then turned on, and a single time-step of one nanosecond was used to obtain the results for the case with TRI. A comparison of the divergences of the radiative heat fluxes is given in Fig. 7(b). It is clear from the figure that TRI causes the regions of strong divergence to become larger and the flame to spread out more into the co-flowing air stream. In other words, the flame, in the presence of TRI, is more strongly emitting than the case without TRI. Since absorption by the surrounding cold regions is relatively small, this implies that the heat loads at the walls should increase as a result of the inclusion of TRI.

A quantity of extreme practical importance is the heat load on the bluff-body. Since the bluff-body is quite small in size, it is adequate to calculate an increase in the average heat flux (rather than the exact heat flux distribution) caused by TRI. In this particular case, the radiative heat flux on the bluff-body was enhanced by 45%, while the total heat flux increased by 35% when TRI is included. The percentage increase in the total heat flux is larger than for the top and bottom walls, because the convective heat fluxes on the bluff-body are relatively small, since in the wake behind the bluff-body the flow velocities are quite small in comparison with the axial velocity of the air stream flowing past the top and bottom walls.

3.2. Effects on inlet equivalence ratio

The absence of a steady-state solution to the problem under consideration poses severe problems in data presentation. When the inlet equivalence ratio, Φ_{in}, for example, is changed, the entire flame structure, and the time history of the flame, changes. Comparing results at any instance of time for the various cases is not at all meaningful since at the same instant of time, the flame structure and turbule locations are completely different for different values of Φ_{in}. Even for the same values of Φ_{in} such a comparison is not meaningful since the time histories are significantly different for the cases with and without radiation (and TRI).

The above difficulty was overcome by a tedious data processing procedure. The steps involved were as follows:

1. Figures, similar to Fig. 5, were plotted for each case with and without TRI.
2. A time-period was determined for each case by careful examination of these plots. Typically they varied between 90 to 120 ms.
3. The data files for each case, which were stored earlier at 10 ms intervals, were averaged over two time periods once it was ascertained that the initial startup period had passed. This procedure yields a time average over two 'periods'.

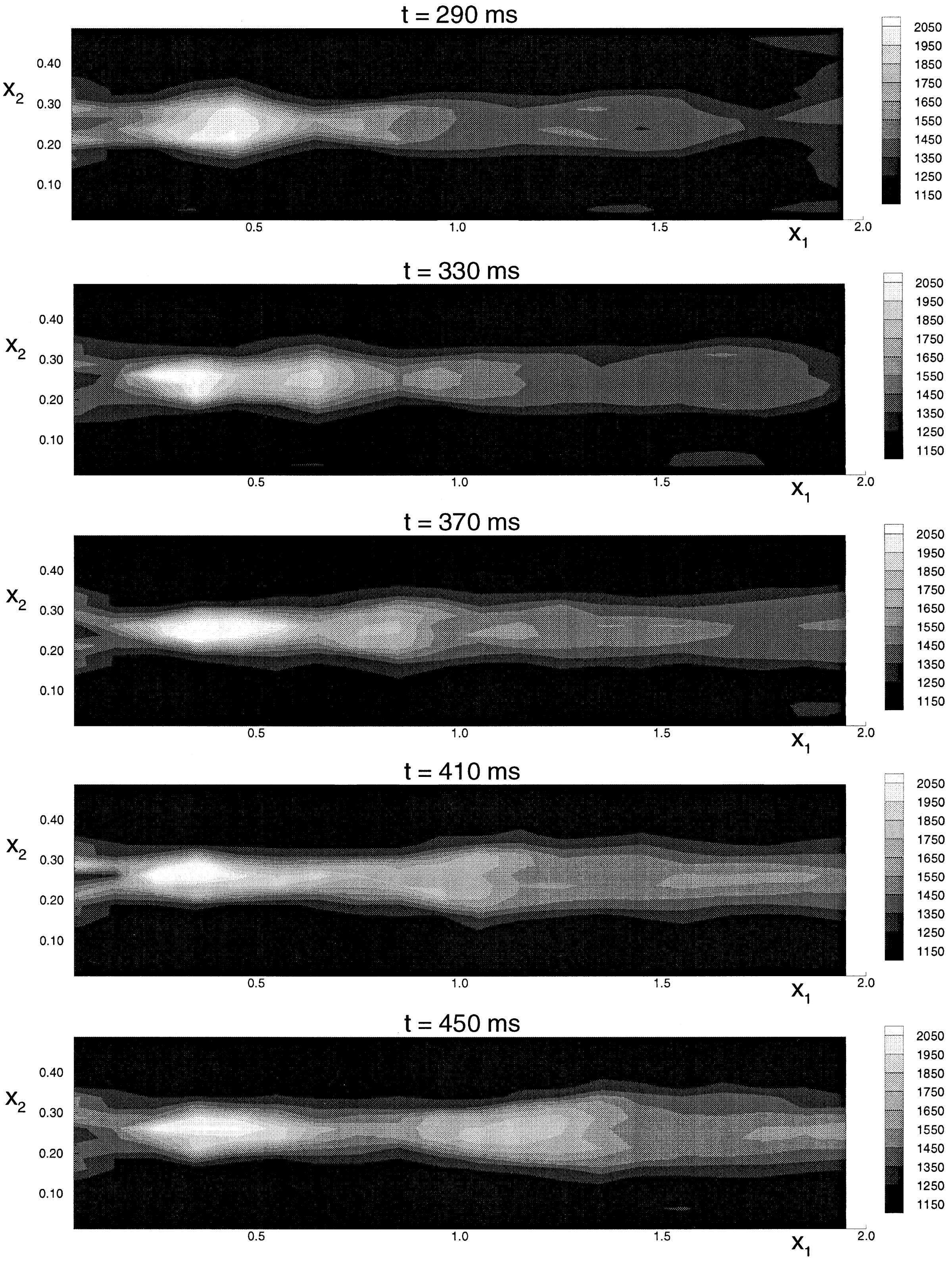

t = 290 ms

t = 330 ms

t = 370 ms

t = 410 ms

t = 450 ms

Fig. 6. Flame structure with radiation and TRI.

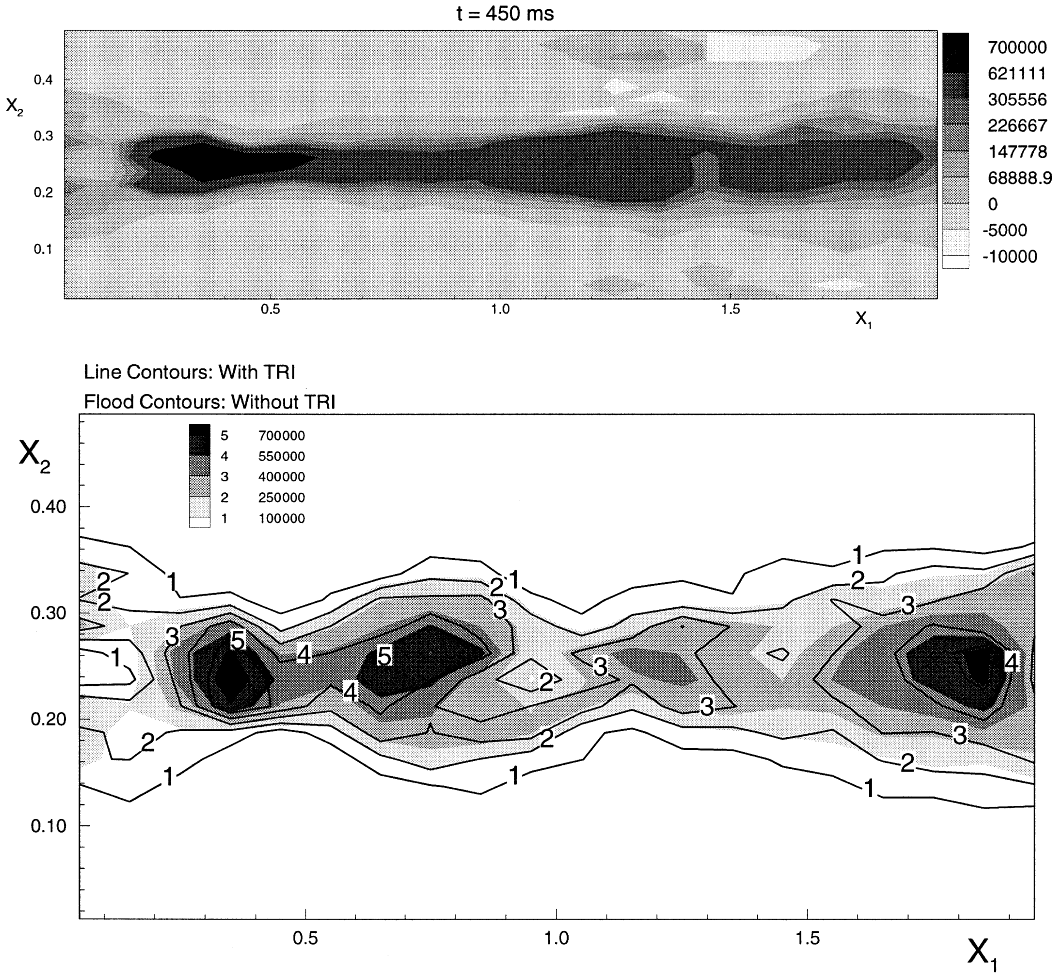

Fig. 7. (a) Divergence of radiative heat flux representative of absorption and emission from the flame; (b) effect of TRI on the divergence of the radiative heat flux.

While the determination of the so-called 'time-period' is somewhat qualitative, this procedure gives a fair average quasi-steady representation of the various cases. In fact, it was found that by performing the same operation over a single period or two periods produced results within 6% for each case. This discrepancy can easily be attributed to the difficulty in determining the exact time-period in each case, and to the fact that this period is not globally true.

The procedure, described above, was used to post-process wall heat flux data for the four different equivalence ratios with and without TRI. The nondimensional convective and radiative wall heat fluxes are depicted in Fig. 8. The heat fluxes have been normalized by $\lambda(\langle T_{a,in}\rangle - T_w)/B$, where λ is the thermal conductivity of the medium (assumed to be that of air at 1200 K), T_w is the wall temperature, $\langle T_{a,in}\rangle$ is the mean inlet air temperature, and B is the size of the bluff-body.

Several important facts are revealed by Fig. 8. First, it shows that irrespective of the equivalence ratio, TRI enhances the radiative heat fluxes at the top and bottom walls by about 40%. Secondly, the radiative heat fluxes, on average, are about 1.6 times larger than the convective heat fluxes without TRI, and about 2.4 times larger when TRI is included. The inclusion of TRI, as shown earlier, makes the flame colder. The impact of TRI, however, is restricted to the hot axial zone of the flame where radiative effects are strong, and where the fluctuations in the temperature and composition fields are large. Convection is a local phenomenon, and the wall convective heat fluxes are a function of only the temperature of the fluid film adjacent to the wall, which is not affected by the changes in the hot axial zone. Consequently, the convective wall heat fluxes at the top and bottom walls remain unaffected by the inclusion of TRI, which is corroborated by Fig. 8.

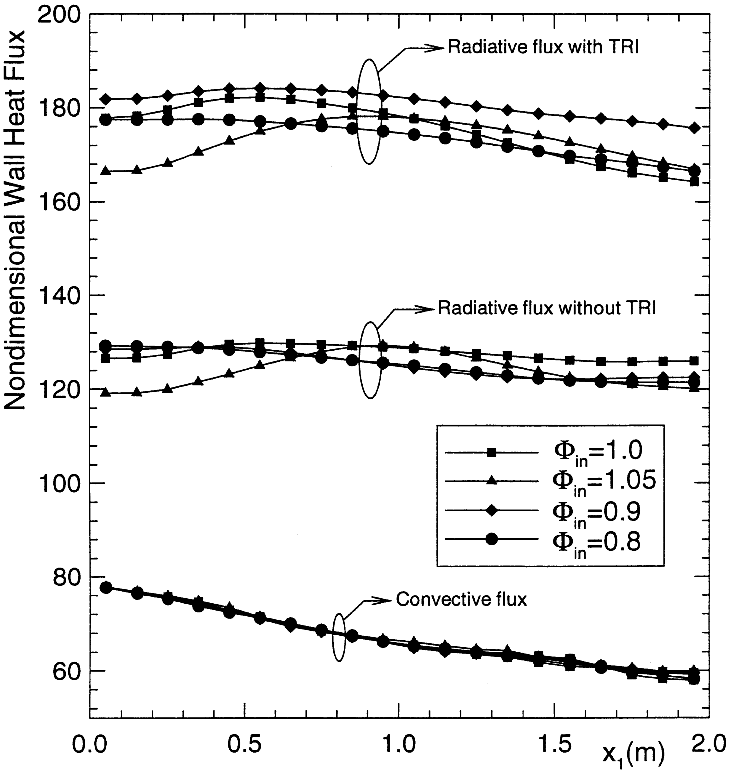

Fig. 8. Nondimensional wall heat fluxes at various inlet equivalence ratios with and without TRI.

The maximum change in the convective heat flux at any location is 3.3%. Another important observation is that the radiative heat flux reaches a peak in the first half of the channel, where the primary hottest combustion zone is always located. Contrary to this observation, the convective heat flux decreases monotonically in the downstream direction.

The nondimensional average heat loads on the bluff-body are tabulated in Table 2. Here too, as for the walls considered earlier, the radiative heat flux is enhanced by about 40% for all equivalence ratios. An interesting trend is observed for the convective heat flux: as the inlet equivalence ratio decreases, the convective heat flux increases. An increase of 35% is observed when comparing equivalence ratios of unity and 0.8, as opposed to almost no change for the top and bottom walls. This is due to the fact that here the equivalence ratio is decreased by decreasing the fuel injection velocity (Table 1). As a result, the temperatures in the wake behind the bluff-body are significantly larger for smaller equivalence ratios. This is illustrated in Fig. 9. Although a single snapshot is shown here, the above observation was made for all times. Rocquemore et al. [30] and Lee and Onuma [31] discusses the structure of the recirculation zone behind the bluff-body for various fuel injection speeds. For slower fuel injection speeds, the recirculation zone behind the bluff-body becomes stronger and assumes an almost spherical shape. Bulk mixing, in such cases, plays a significant role. Consequently, convective heat transfer behind the bluff-body becomes stronger. This is reflected in Table 2, where a distinct increase in convective heat flux is noted for smaller values of Φ_{in} (slower flow). For small equivalence ratios, it is also observed that TRI decreases the convective heat flux by about 9%, as opposed to the maximum of 3% that was noted for the top and bottom walls. Inclusion of TRI decreases the

Table 2
Nondimensional average heat loads on the bluff-body at various inlet equivalence ratios

Φ_{in}	$\underline{q}_w^R$ without TRI	$\underline{q}_w^R$ with TRI	$\underline{q}_w^C$ without TRI	$\underline{q}_w^C$ with TRI
1.05	110.6	155.2	27.6	26.9
1.0	115.5	163.6	31.3	30.1
0.9	115.8	164.7	38.9	35.5
0.8	117.6	159.4	48.0	43.8

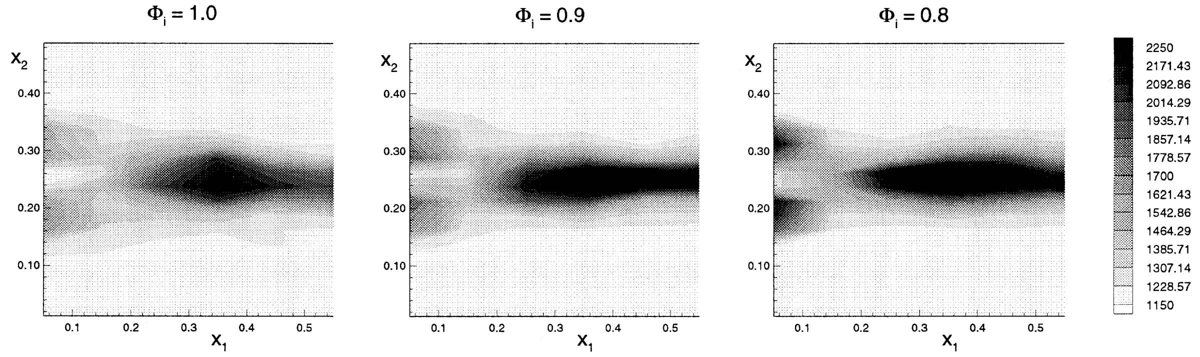

Fig. 9. Temperature contours in the wake of the bluff-body for various equivalence ratios after 450 ms.

temperatures, and due to stronger mixing (than near the top and bottom walls) behind the bluff-body, the convective heat load on the bluff-body is affected.

3.3. Effects of Reynolds number

Thus far, the discussion has been limited to a single Reynolds number. For this baseline *Re* equal to 13,304, it was found that the radiative fluxes dominated the convective fluxes. As the Reynolds number is increased, convective fluxes are expected to become more and more dominant. The relative magnitude of the convective and radiative heat loads has always been an important issue in burner design and, therefore, the Reynolds number is definitely an important parameter. Computations were performed at three different Reynolds numbers (Cases 13–18). All calculations were performed at a baseline equivalence ratio of unity. Two noticeable trends are observed. First, as the Reynolds number is increased, the flame on an average gets colder. Secondly, as the Reynolds number is increased, the flame seems to extinguish completely in the neck region before reigniting further downstream. This is a typical experimentally observed phenomenon.

Figure 10 shows the nondimensional radiative and convective wall heat fluxes at various Reynolds numbers. As discussed earlier, with an increase in the Reynolds number, the flame gets colder and consequently, the radiative heat fluxes decrease both with and without TRI. The convective heat fluxes, on the other hand, increase with an increase in the Reynolds number in accordance with earlier expectations. For the two higher *Re*, convective and radiative wall heat loads contribute almost equally to the next heat flux. The effect of TRI, once again, is to substantially enhance the radiative heat loads, and cause insignificant changes in the convective heat loads. Although the radiative heat fluxes decrease with increasing *Re*, the enhancement of the radiative heat fluxes caused by TRI is almost constant if absolute magnitudes are considered and, in fact, larger at higher *Re* if the enhancement is expressed as a percentage of the radiative heat flux without TRI. The fact that the effect of TRI is almost constant even if the flame is cold, suggests that its role can, by no means, be overlooked or ignored. It TRI is included, the extinction of the flame, for example, would take place at relatively lower flow speeds that for the case where TRI is not taken into account.

The heat loads on the bluff-body have been tabulated in Table 3 for various Reynolds numbers. Here too, as was the case for the top and bottom walls, the radiative heat fluxes decrease with an increase in the Reynolds number. The magnitude of the radiative heat fluxes on the bluff-body are still much larger than the convective heat fluxes. Although the convective heat fluxes on the bluff-body increase with an increase in *Re*, even for the highest *Re*, its magnitude is substantially smaller than the radiative heat fluxes, especially if TRI is taken into account.

If the total heat load (convective + radiative) on the bluff-body is considered, Table 3 reveals that without the inclusion of TRI, the net heat flux decreases by about 10% when the Reynolds number is increased threefold, while it decreases only by about 2% if TRI is included. This, of course, is in addition to the fact that with TRI the neat heat loads are much larger. These observations lead to the conclusion that if TRI is included, the bluff-body is susceptible to much larger heat loads at a wide range of Reynolds numbers.

3.4. Numerical issues

Two issues are of particular interest here: (1) the computational effort which was required to solve the problem under consideration, and (2) the statistical errors associated with the results presented in the preceding sections.

Apart from its ability in being able to resolve the various interactions in a reactive flow problem, the PDF Monte Carlo method has the advantage of being able to produce worthwhile results within the limitations of a

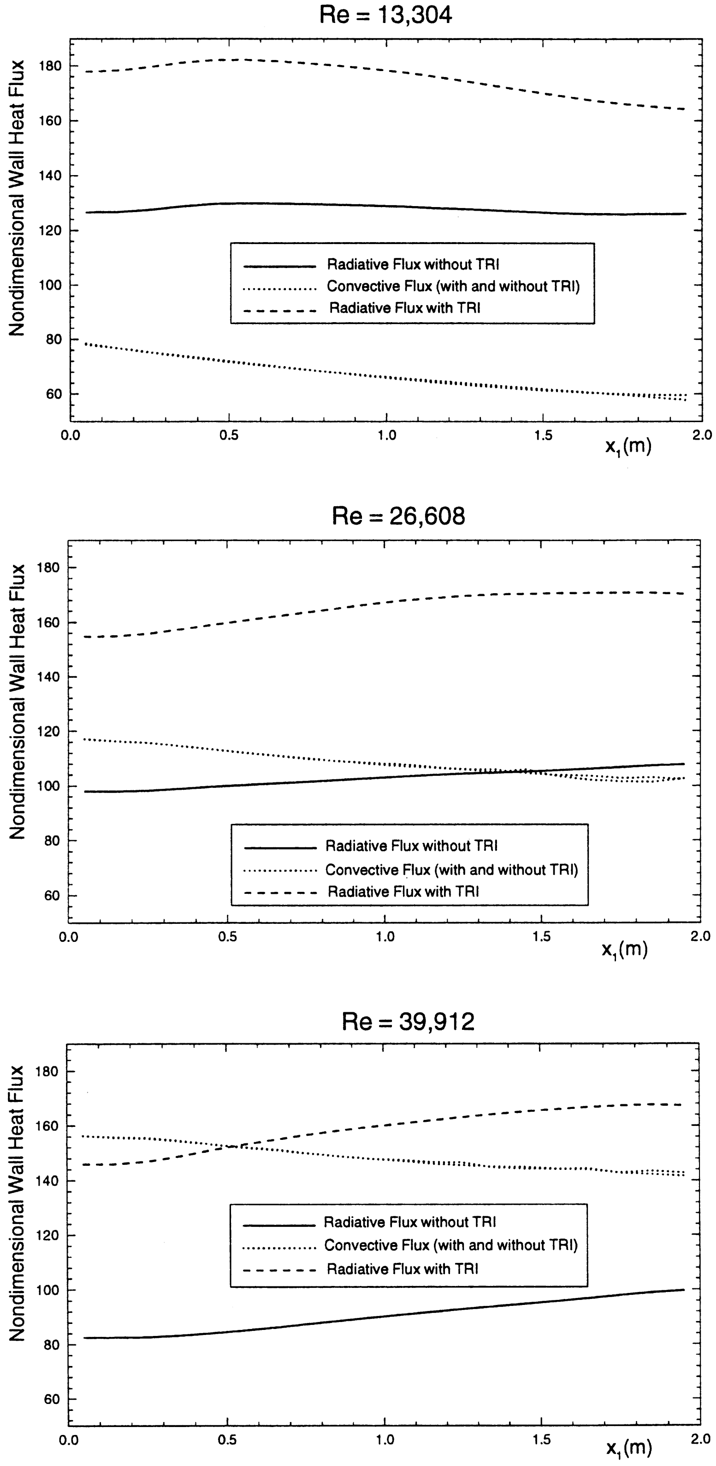

Fig. 10. Nondimensional wall heat fluxes at various Reynolds numbers.

Table 3
Nondimensional average heat loads on the bluff-body at various Reynolds numbers

Re	$\underline{q}_w^R$ without TRI	$\underline{q}_w^R$ with TRI	$\underline{q}_w^C$ without TRI	$\underline{q}_w^C$ with TRI
13,304	115.5	163.6	31.3	30.1
26,608	91.1	144.8	45.0	44.9
39,912	77.9	136.8	53.7	53.0

standard single-processor workstation. For the current study, since the problem under consideration does not have a steady state solution, a budget of the CPU consumed during a single time step was constructed. Table 4 shows the CPU consumed by each process within a time step expressed as a percentage of the total CPU consumed during the time step. The total CPU time required for a single time step calculation was 96 s (for Case 3) on a 195 MHz, single-processor R10000 Silicon Graphics Indigo2 computer, which suggests that a 400 time-step job would require approximately 11 h. It is evident from Table 4 that the solution of the reaction rate equations constitute a major fraction of the total CPU time.

The statistical uncertainties were estimated for the results presented earlier. This was done by computing Case 3 up to 250 ms ten different times. For each run, a different set of starting random number seeds were used. The mean of all quantities at all spatial locations were stored from all ten runs. They were finally averaged to provide the mean of the means at all spatial locations. The deviation of the individual data sets from the mean of the mean provided the standard deviation (or uncertainty). The uncertainties were computed separately for each species. Figures 11 and 12 show the statistical errors associated with the calculation of temperature and methane concentrations. For temperature, uncertainties are shown along the channel centerline and for a cross-section at $x_1 = 0.4$ because these are sections where the chemical reaction is strong, and where the bulk of the action takes place. Since a single-step reaction has been used, production of heat is directly correlated to production of CO_2 and, therefore, the uncertainties for CO_2 concentrations are almost identical to those of temperature (not shown). For methane, a cross-section at $x_1 = 0.15$ is depicted because this was observed to be the section of maximum uncertainty. Furthermore, this location corresponds to $x_1/D \simeq 10$, which is the so-called 'neck' of the flame, and the location at which the sporadic injection of methane (discussed earlier) occurs.

Table 4
CPU budget for a single time step

Calculation performed	% of total CPU
Radiative property	3.61
Averaging	8.92
Solution of RTE	4.44
Printing output	0.22
Smoothing and derivatives	1.26
Explicit integration	8.45
Boundary treatment	8.15
Chemical reaction	63.27
Miscellaneous	1.67
Total CPU	96 s

4. Summary and conclusions

A novel approach for the computation of turbulent reactive flows including radiation has been presented. The velocity-composition joint PDF is a unique approach that can resolve the various interactions between turbulence, chemical reaction and radiative transfer. In the current study, the method has been applied to a two-dimensional bluff-body burner. It has been established that the method is a powerful tool in resolving the above-mentioned interactions.

The results may be summarized as follows:

1. The experimentally observed turbule shedding phenomenon, the stretching of the flame, and the sporadic injection of fuel into the primary combustion zone were, at least qualitatively, reproduced by the current code.
2. It was observed that radiation resulted in the flame being about 250 K colder, on the average, than a non-radiating flame. When turbulence–radiation interactions (TRI) were included, the flame temperatures decreased by an additional 100 K. Turbulence–radiation interactions enhance emission from the flame, and since the bulk of the gas within the combustor is optically thin, stronger flame emission results in an increase in wall radiative heat loads.
3. The increase in radiative heat fluxes due to TRI was almost the same at all inlet equivalence ratios for a baseline Reynolds number of 13,304. In each case the radiative heat flux at the top and bottom walls, as well as the bluff-body, increased by about 40–45% when TRI was included. The convective heat fluxes at the top and bottom walls remained unchanged when TRI was included, and were also observed to be the same at various inlet equivalence ratios. Since the inlet equivalence ratio was adjusted by adjusting the fuel injection speed, noticeable differences were observed

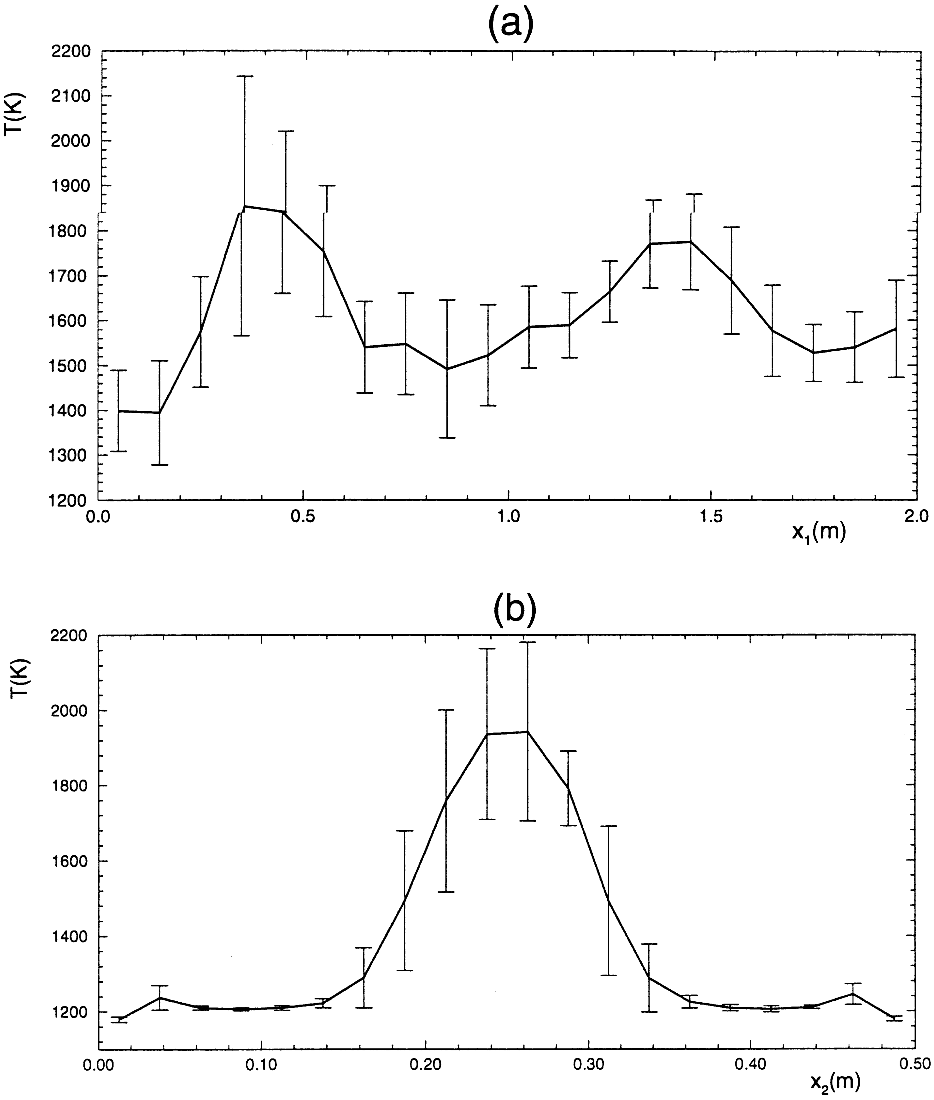

Fig. 11. Statistical errors associated with temperature: (a) temperature along channel centerline ($x_2 = 0.25$ m) with uncertainties, and (b) temperature along a cross-section cut at $x_1 = 0.4$ m with uncertainties.

in temperature distributions close to the bluff-body at various inlet equivalence ratios. At smaller inlet equivalence ratios (smaller fuel injection speeds), the convective heat leads on the bluff-body were observed to be larger. In addition, the inclusion of TRI was observed to decrease the convective heat loads on the bluff-body.

4. With an increase in Reynolds number, the flame became colder, and consequently, the radiative wall fluxes decreased. On the other hand, the convective wall heat fluxes increased with Reynolds number. When TRI was included, the radiative wall heat fluxes were enhanced by almost the same absolute values for all Reynolds numbers, although the net radiative flux was smaller for larger Reynolds numbers. At higher Reynolds numbers, the peak heat fluxes were also observed to shift further downstream.
5. The statistical errors associated with the calculations were reported. It was found that the errors were highest in regions of strong chemical reaction and radiation, the highest being in the order of about 16%.

Lagrangian methods are extremely suitable for distributed computing and provide highest returns when used for complex problems. With the increase in the size and complexity of engineering problems dealt with today,

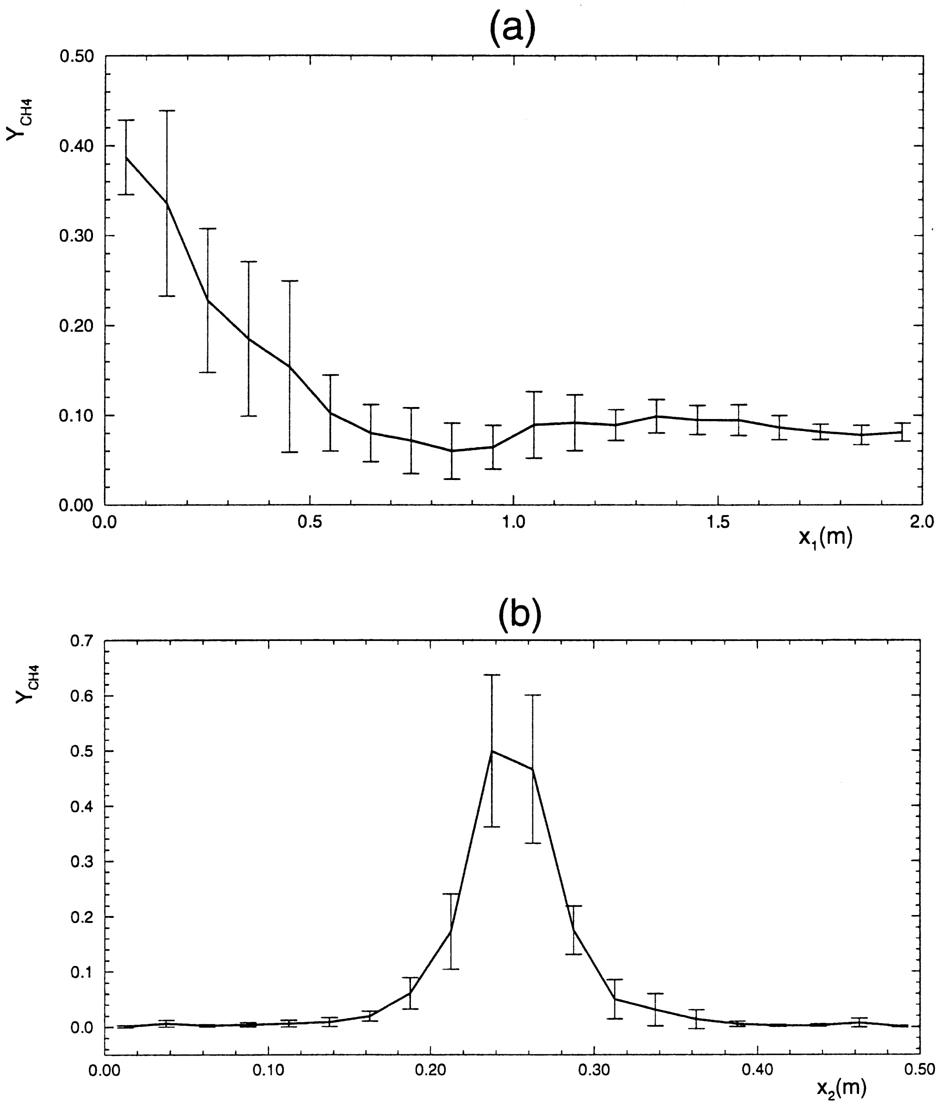

Fig. 12. Statistical errors associated with CH_4 concentrations: (a) CH_4 mass-fraction along channel centerline ($x_2 = 0.25$ m) with uncertainties, and (b) CH_4 mass-fraction along a cross-section cut at $x_1 = 0.15$ m with uncertainties.

it appears that novel techniques, such as the one outlined here, are becoming more of a necessity than a mere option. Hopefully, the advantages and benefits of using the velocity-composition joint PDF method have been emphasized and highlighted enough to lure the reader into adopting the current approach in his or her research.

Acknowledgements

The authors wish to thank the Applied Research Laboratory at Penn State for partial funding of this research. The first author also wishes to thank Dr Stephen R. Turns for his suggestions on the combustion aspects of the problem, Dr Timothy F. Miller for his help with CFD issues, and Silicon Graphics Inc. for sharing their computational resources.

References

[1] G. Cox, On radiant heat transfer from turbulent flames, Combustion Science and Technology 17 (1977) 75–78.
[2] S.E. Elghobashi, W.M. Pun, A theoretical and experimental study of turbulent diffusion flames in cylindrical furnaces, Fifteenth Symposium (International) on Combustion/The Combustion Institute, 1974, p. 1353.
[3] V.P. Kabashnikov, G.I. Myasnikova, Thermal radiation in

turbulent flows—temperature and concentration fluctuations, Heat Transfer—Soviet Research 17 (6) (1985) 116–125.

[4] V.P. Kabashnikov, Thermal radiation in turbulent flows—in the case of large fluctuations of the absorption coefficient and the Planck function, Journal of Engineering Physics 49 (1) (1985) 778–784.

[5] V.P. Kabashnikov, G.I. Kmit, Influence of turbulent fluctuations on thermal radiation, J. Appl. Spectrosc. 31 (1979) 963–967.

[6] B.E. Pearce, A.K. Varma, Radiation–turbulence interaction in a tactical missile exhaust plume, AIAA Paper (81–1110), 1981.

[7] M. Germano, turbulent fluctuations coupled with the radiation field, AIAA Paper (78–840), 1978.

[8] R.J. Hall, A. Vranos, Efficient calculations of gas radiation from turbulent flames, Int. J. Heat Mass Transfer 87 (17) (1994) 2745–2750.

[9] A. Soufiani, P. Mignon, J. Taine, Radiation–turbulence interaction in channel flows of infrared active gases, Proceedings of the International Heat Transfer Conference 6 (1990) 403–408.

[10] T.H. Song, R. Viskanta, Interaction of radiation with turbulence: application to a combustion system, Journal of Thermophysics 1 (1) (1987) 56–62.

[11] S.H. Chan, C.F. Chern, A method for turbulence–radiation interaction analysis in multiphase liquid metal diffusion flames, Proceeding of the Ninth International Heat Transfer Conference, Jerusalem, Israel 4 (11-J-04) 1990, pp. 143–148.

[12] J.P. Gore, S.M. Jeng, G.M. Faeth, Spectral and total radiation properties of turbulent carbon-monoxide/air diffusion flames, AIAA Journal 25 (2) (1987) 339–345.

[13] M. Kounalakis, Y. Sivathanu, G.M. Faeth, Infrared radiation statistics of nonluminous turbulent diffusion flames, ASME/JSME Thermal Engineering Proceedings 5 (1991) 3–12.

[14] J.R. Gore, S.M. Jeng, G.M. Faeth, Spectral and total radiation properties of turbulent hydrogen/air diffusion flames, Journal of Heat Transfer 109 (1987) 165–171.

[15] S.M. Jeng, M.C. Lai, G.M. Faeth, Nonluminous radiation in turbulent buoyant axisymmetric flames, Combustion Science and Technology 40 (1984) 41–53.

[16] B.R. Adams, P.J. Smith, Modeling effects of soot and turbulence–radiation coupling on radiative transfer in turbulent gaseous combustion, Combustion Science and Technology 109 (1995) 121–140.

[17] S. Mazumder, Numerical study of chemically reactive turbulent flows with radiative heat transfer, Ph.D. Thesis in Mechanical Engineering, The Pennsylvania State University, 1997.

[18] S.B. Pope, Computations of turbulent combustion: progress and challenges, Twenty-Third symposium (International) on Combustion/The Combustion Institute, 1990, pp. 591–612.

[19] S.B. Pope, PDF methods for turbulent reactive flows, Progress in Energy and Combustion Science 11 (1985) 119–192.

[20] M.F. Modest, Radiative Heat Transfer, McGraw-Hill, 1993.

[21] D.C. Haworth, S.B. Pope, A PDF modeling study of self-similar turbulent free shear flows, Physics of Fluids 30 (1987) 1026–1044.

[22] C. Dopazo, Probability density function approach for a turbulent axisymmetric heated jet. Centerline evolution, Physics of Fluids 18 (4) (1975) 397–404.

[23] S. Mazumder, M.F. Modest, A stochastic Lagrangian model for near-wall turbulent heat transfer, ASME Journal of Heat Transfer 119 (1) (1997) 46–52.

[24] S. Mazumder, M.F. Modest, Boundary treatment and an efficient pressure algorithm for internal turbulent flows using the PDF method, International Journal for Numerical Methods in Fluids 24 (1997) 215–232.

[25] C.K. Westbrook, F.L. Dryer, Simplified reaction mechanisms for the oxidation of hydrocarbon fuels in flames, Combustion Science and Technology 27 (1981) 31–43.

[26] C.W. Gear, Numerical Initial-Value Problems in Ordinary Differential Equations, Prentice-Hall, Englewood Cliffs, NJ, 1971.

[27] D.K. Edwards, Molecular gas band radiation, Advances in Heat Transfer 12 (1976) 115–193.

[28] A.T. Modak, Exponential wide band parameters for the pure rotational band of water vapor, J. Quant. Spectrosc. Rad. Transfer 21 (1979) 131–142.

[29] M.F. Modest, K.K. Sikka, The Stepwise Gray P-1 Approximation for multi-dimensional radiative transfer in molecular-gas–particulate mixtures, J. Quant. Spectrosc. Rad. Transfer 48 (2) (112) (1992) 159–168.

[30] W.M. Roquemore, R.L. Britton, S.S. Sandhu, Dynamic behavior of a bluff-body diffusion flame, AIAA Journal 21 (10) (1983) 1410–1417.

[31] C.E. Lee, Y. Onuma, Experimental study of turbulent diffusion flames stabilized on a bluff body, JSME International Journal, Series B 37 (1) (1994) 165–171.

[32] A.R. Masri, R.W. Bilger, Turbulent diffusion flames of hydrocarbon fuels stabilized on a bluff body, Twentieth Symposium (International) on Combustion, 1984, p. 319.

[33] J.T. Kelly, M. Namazian, R. Schefer, Bluff-body burner flows, fuel concentrations, and flame regimes, Transactions of the ASME: Fossil Fuel Combustion PD-25, 1988, pp. 7–12.

[34] M. Namazian, J.T. Kelly, R. Schefer, Near-field instantaneous flame and fuel concentration structures, Twenty-Second Symposium (International) on Combustion/The Combustion Institute, 1988, pp. 627–634.

[35] C.M. Rhie, W.L. Chow, Numerical study on the turbulent flow past an airfoil with trailing edge separation, AIAA Journal 21 (11) (1983) 1525–1532.

[36] R.I. Issa, Solution of the implicitly discretised fluid flow equations by operator-splitting, Journal of Computational Physics 62 (1985) 40–65.

[37] F.M. White, Viscous Fluid Flow, McGraw-Hill, 1991.

[38] C.H.K. Williamson, Three-dimensional vortex dynamics in bluff body wakes, Experimental Thermal and Fluid Science 12 (1996) 150–168.

[39] S.M. Correa, A. Gulati, S.B. Pope, Raman measurements and joint PDF modeling of a nonpremixed bluff-body-stabilized methane flame, Twenty-fifth Symposium (International) on Combustion/The Combustion Institute, 1994, pp. 1167–1173.